Energy & Environmental Science

ROYAL SOCIETY OF CHEMISTRY

PAPER

View Article Online
View Journal | View Issue

Cite this: *Energy Environ. Sci.*, 2025, **18**, 4690

The spontaneous cascade optimization strategy of the double enrichment improves anion-derived solid electrolyte interphases to enable stable lithium-metal batteries†

Fengxu Zhen,‡[a] Hong Liu,‡[a] Yingbin Wu,‡[a] Xinjia Zhou,[a] Weiping Li,[a] Yuzhi Chen,[a] Yuke Zhou,[a] Haoyang Wang,[a] Xiangkai Yin,[a] Shujiang Ding,*[a] Xiaodong Chen*[b] and Wei Yu*[a]

Anion regulation represents a highly effective, convenient, and economical approach to generate LiF-rich solid electrolyte interfaces (SEIs). The anion decomposition process is influenced by charge density and anion concentration. However, current research primarily concentrates on increasing charge density to enhance anion decomposition. Herein, the spontaneous cascade optimization strategy driven by the double enrichment of anions and charges is proposed by utilizing NH_2-MIL-101(Fe)@Copc (MOF@Copc). Specifically, NH_2-MIL-101(Fe) functions as a $TFSI^-$ anion trap *via* the Lewis acid–base interactions and synergistic hydrogen bonding, thereby achieving primary optimization. Subsequently, the rich electronic structure of Copc facilitates charge delocalization and lowers the energy barrier for anion decomposition, allowing the C–F bonding to break more readily, thereby enabling further optimization. The π–π stacking interaction between the MOF and Copc facilitates the close association of adsorption and catalytic sites, allowing the continuous breakdown of the C–F series products in a chain reaction. The assembled LFP (19.26 mg cm^{-2}) demonstrates a commercial-grade cathode area capacity, maintaining over 90% capacity retention across 350 cycles at 1C, with a capacity decay rate of only 0.02% per cycle. More importantly, this strategy enables the industrial-scale production of Ah-class anode-free lithium-metal pouch batteries exceeding 300 W h kg^{-1}. Optimizing anion decomposition provides a novel perspective to advance the practical application of lithium-metal batteries.

Received 2nd March 2025,
Accepted 2nd April 2025

DOI: 10.1039/d5ee01219h

rsc.li/ees

Broader context

Lithium metal batteries (LMBs), due to their exceptionally high energy density, are considered one of the most promising energy storage technologies. However, challenges such as dendrite formation and fragile solid electrolyte interphase (SEI) hinder the practical application of LMBs. Here, we present a multi-stage alternating arrangement of adsorption and catalytic sites—NH_2-MIL-101(Fe)@Copc (MOF@Copc), which achieves a significant increase in the LiF content by regulating the mode of 'enrichment-decomposition behavior' of an anion. The content of LiF in the SEI is positively correlated with its cycle life. Therefore, under the lowest N/P conditions, the MOF@Copc/Cu anode-free lithium metal pouch battery demonstrates outstanding long-cycle stability. The protective layer contributes to simultaneously accelerating the development and deployment of high-energy-density LMBs and AFLMBs.

Introduction

Lithium metal, recognized for its high theoretical capacity (3860 mA h g^{-1}) and low redox potential (3.04 V lower than that of the standard hydrogen electrodes), has garnered significant attention.[1,2] The highly reactive lithium metal interacts uncontrollably with the liquid electrolyte, inevitably leading to the formation of solid electrolyte interfaces (SEIs).[3,4] The natural SEI is composed predominantly of organic substances (lithium alkyl carbonates) and contains lower amounts of

[a] *School of Chemistry, Engineering Research Center of Energy Storage Materials and Devices, Ministry of Education, State Key Laboratory of Electrical Insulation and Power Equipment, Xi'an Jiaotong University, Xi'an, 710049, P. R. China. E-mail: dingsj@mail.xjtu.edu.cn, yuwei2019@mail.xjtu.edu.cn*

[b] *Xi'an Institute of Optical Precision Machinery, Chinese Academy of Sciences, Xi'an Shanxi, 710000, P. R. China. E-mail: cxd_1979@163.com*

† Electronic supplementary information (ESI) available. See DOI: https://doi.org/10.1039/d5ee01219h

‡ Co-first author.

inorganic substances (LiF, Li_3N, *etc.*).[5] However, the resulting SEI is structurally inhomogeneous and prone to fragmentation, leading to ruptures during continuous lithium stripping/deposition, and the rupture sites are highly prone to the formation of lithium dendrites, which in turn initiates a series of vicious cycles.[6–11] LiF, possessing exceptional chemical and mechanical stability as well as a low Li^+ diffusion barrier, is widely recognized as a key component in constructing a stable SEI.[12,13]

Currently, the primary strategies to enhance the LiF content in SEIs involve the addition of fluorinated solvents, the construction of a high-concentration electrolyte, and the use of electrolyte additives. However, these strategies exhibit certain limitations in practice: most fluorinated solvents tend to generate corrosive HF and decomposition by-products (CH_3OH), which accelerate the deterioration of the electrode interface.[14,15] The high concentration of electrolyte is at the expense of a good solid–liquid contact interface,[16] while fluorinated electrolyte additives incur high costs.[17] The formation of LiF relies heavily on the decomposition of fluorine-containing compounds.[18] Therefore, the modulation of fluorine-containing anions is expected to construct the *in situ* LiF-SEI without altering the electrolyte composition. However, the inability to generate an effective SEI layer on the lithium metal surface is attributable to two underlying reasons: (1) A limited number of anions at the electrode surface. The electric field, driven by the charging conditions, promotes anion migration toward the cathode electrode, thereby exacerbating the formation of an anion–deficient interface. (2) Slow electron transport kinetics. Lithium bis(trifluoromethanesulfonyl)imide (LiTFSI), characterized by its numerous C–F fragments and high ion conductivity, is considered a promising candidate for replacing $LiPF_6$.[19] However, since the decomposition of LiTFSI is electron-driven, the slow electron transfer kinetics hinder the anions from acquiring sufficient charge. This limitation leads to the formation of an SEI primarily composed of CF_3^-, which represents an incomplete reduction product of $TFSI^-$.[20–23] Therefore, the anionic decomposition process is constrained by a limited number of anions and a finite amount of electrical charge. Recent research has consistently demonstrated that optimizing electron-directed transport kinetics can effectively increase the degree of $TFSI^-$ decomposition. Gao *et al.* reported that Li–Au alloys produced by *in situ* lithiation possess significant electron-donating properties, thus facilitating the decomposition of LiTFSI within the electrolyte.[24] Liu *et al.* enhanced the electron transfer kinetics using a Br-TPOM skeleton with high electron transfer capacity, thereby promoting the breakup of the C–F bond and leading to the formation of LiF.[25] In parallel, Liu *et al.* constructed a "charge warehouse" using a porphyrin-organic framework (POF), serving as a charge source and ensuring sufficient charge transfer for the $TFSI^-$, thereby facilitating the formation of a LiF-rich SEI layer.[26] However, these studies primarily focus on the charge enrichment while overlooking the enrichment of anions. Addressing only one of these factors will not fully maximize anionic decomposition. Therefore, simultaneously enriching anions and enhancing electron transfer kinetics constitute effective methods for forming an excellent LiF-rich SEI.

Herein, a spontaneous cascade optimization strategy is proposed through the design of the NH_2-MIL-101(Fe) @Copc composite material (Fig. 1). The central Fe^{3+} ion, featuring an empty orbital, participates in the Lewis acid–base interaction with $TFSI^-$, which possesses lone pair electrons. Owing to the synergistic effects of Lewis acid–base interactions and the formation of hydrogen bonds with amino groups, precisely anchoring the wandering $TFSI^-$ ions to concentrate them on the surface of the modified layer, thus achieving initial optimization of anion-rich interfaces. Simultaneously, cobalt phthalocyanine (Copc) characterized by its electron-rich conjugated structure, creates an electron-rich environment through electron delocalization. An electron-rich environment is advantageous as it facilitates the formation of more coherent electron transport pathways, thus reducing the energy barriers faced by electrons during intermolecular transfer. The anion decomposition is facilitated by enhancing the electron transport kinetics. The two optimizations within the cascade strategy guarantee the efficient decomposition of the anions by the double enrichment of anions and charges.

To validate the efficacy of the cascade optimization strategy, we constructed a MOF@Copc layer to serve as the artificial solid

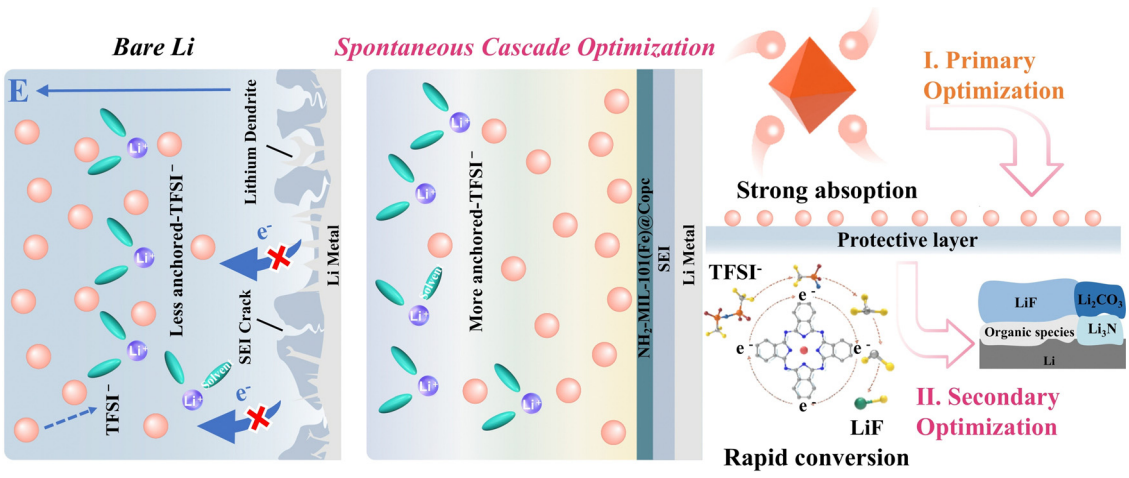

Fig. 1 Schematic diagram of the principle of the modification layer NH_2-MIL-101(Fe)@Copc.

electrolyte interface (ASEI). Benefiting from the advancement of this strategy, the synergistic combination yields an increase in the LiF content from 30.2% to 41.7%. Impressively, Li–Cu half-cells modified with MOF@Copc exhibited stable cycling for more than 650 cycles, while maintaining an average coulombic efficiency (CE) of 98.85% under test conditions 1 mA cm^{-2}. Meanwhile, MOF@Copc/Li||$LiFePO_4$ (approximately 11.05 mg cm^{-2}), showed a capacity retention exceeding 90% after 1000 cycles at 1C, surpassing the performance reported in most literature reports on artificial SEI strategies. Also, the lifespan of anode-free Li metal pouch cells, with an energy density of 300 W h kg^{-1}, can be extended by nearly four times. This study aims to significantly improve the cycle life of lithium metal batteries by maximizing anion decomposition to form LiF-rich SEIs.

Results and discussion

As shown in Fig. 2a, cobalt phthalocyanine(II) exhibits the strongest signals near the Fermi level, which theoretically

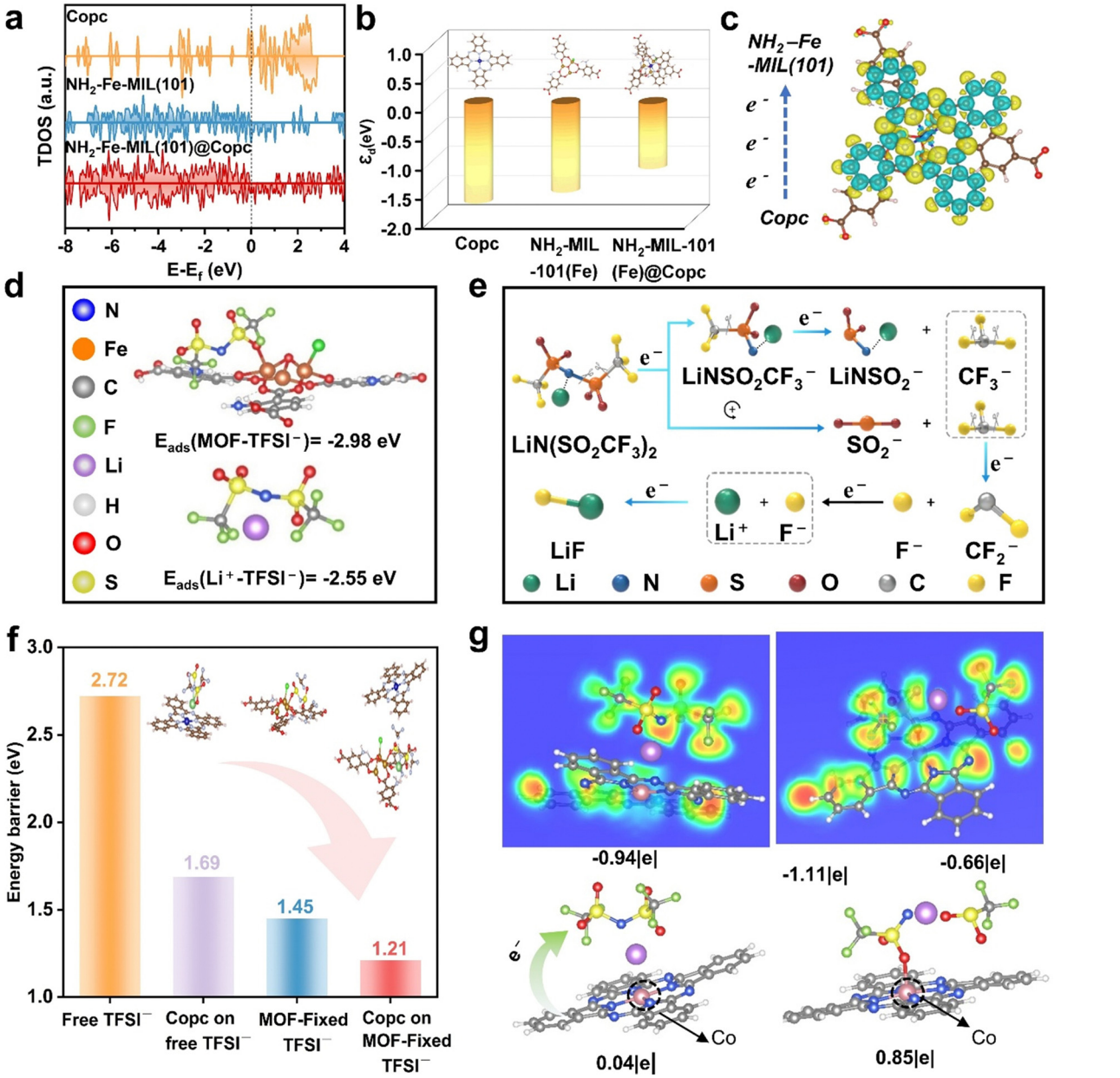

Fig. 2 Mechanism of spontaneous cascade optimization strategy of MOF@Copc modified layer (a) total DOS(TDOS) for Copc, NH_2-Fe-MIL(101) and NH_2-Fe-MIL(101)@Copc. (b) ε_d of Copc, NH_2-Fe-MIL(101) and NH_2-Fe-MIL(101)@Copc. (c) Differential charge density diagram. (d) Binding energy of $TFSI^-$ with MOF and Li^+ interactions. (e) LiTFSI decomposition mechanism. (f) The decomposition energy barrier of the rate-determining step of $TFSI^-$ under the conditions of MOF, Copc alone, and their synergistic collaboration. (g) DFT simulations with Bader charges (measured in units of |e|) illustrate the degradation dynamics of $TFSI^-$, along with the corresponding ELF of $TFSI^-$ at various steady states.

suggests good conductivity. However, its tendency for spontaneous aggregation, combined with its poor film-forming properties, restricts its broader application as an artificial protective layer. Therefore, composite material NH_2-Fe-MIL(101)@Copc can effectively regulate the dispersion of Copc clusters while ensuring great electrical conductivity. Additionally, as shown in Fig. 2b, the upward shift of the d-band center at the active sites strengthens the interaction with $TFSI^-$ anions, consistent with the adsorption energy results presented in Fig. 2d. Subsequently, (Fig. 2c) the calculation and analysis of differential charge densities reveal a significant charge difference between the two materials, with the directional transfer of electrons from cobalt phthalocyanine to the MOF.

According to Fig. 2e, the decomposition reaction of LiTFSI is divided into four distinct stages, each of which is induced by electrons, ultimately resulting in the formation of LiF. This indicates that the degree of $TFSI^-$ decomposition can be optimized through electron-directed conduction. Cobalt phthalocyanine is characterized as a conjugated system with an 18 π electronic structure, where the two –NH– groups each contribute two electrons, while the remaining nitrogen and carbon atoms each donate one electron. We traced the four-step decomposition reaction of $TFSI^-$ using first-principles calculations (Fig. 2g and Fig. S1, ESI†). Bader charge analysis reveals that a 0.83 e^- charge is transferred from the ''electronic dark cloud'' cobalt phthalocyanine to the $TFSI^-$ anion, resulting in N–S splitting. Subsequently, the CF_3^- group detaches from the $SO_2CF_3^-$ ionic fragments as the anion gains additional charges. The CF_3^- group then decomposes further into CF_2^- and F^-. Ultimately, the F^- ion combines with Li^+ to form LiF. In addition, we investigated the effect of the cobalt phthalocyanine on the degree of $TFSI^-$-dissociation using density-functional theory (DFT) (Fig. S2, ESI†) and detailed the changes in the C–F bond in Table S1 (ESI†). In the initial state, the C–F bonds of TFSI-anions are 1.343 Å, 1.344 Å, and 1.346 Å, respectively. Following electron transfer interactions with phthalocyanine, the bond lengths extended to 1.363 Å, 1.351 Å, and 1.350 Å, respectively. Cobalt phthalocyanine, due to its electron-rich nature, has been shown to weaken the interaction force between C and F atoms. The easier breakage of the C–F bond generates more LiF. Finally, the synergistic effect between Copc and MOF was further elucidated through the calculation of the decomposition energy barriers using DFT (Fig. 2f and Table S2 and Fig. S3a and b, ESI†). The calculation results demonstrate that Copc can lower the decomposition potential barrier of anions. Furthermore, $TFSI^-$ decomposition is further enhanced by the combined effects of charge transfer facilitated by Copc and anchoring by MOF.

NH_2-MIL-101(Fe) was successfully synthesized using a straightforward hydrothermal synthesis strategy (Fig. 3a). Subsequently, NH_2-MIL-101(Fe)@CoPc composites were synthesized *via* the impregnation method. The planar π-conjugated structure Copc causes molecular aggregation through π–π stacking.[27] DFT calculations confirm that the binding energy between NH_2-MIL-101(Fe) and Copc is lower than that between Copc molecules alone (Fig. S4, ESI†), suggesting that the stronger π–π interaction between NH_2-MIL-101(Fe) and Copc is thermodynamically favorable. The NH_2-MIL-101(Fe)@Copc composite material not only addresses the issue of spontaneous Copc aggregation but also ensures uniform and firm dispersion of Copc molecules on the iron-based metal–organic framework.[28]

The chemical structures of NH_2-MIL-101(Fe), and NH_2-MIL-101(Fe)@CoPc nanocomposites were analyzed using FT-IR spectroscopy (Fig. 3f). A broad absorption peak at 3368 cm^{-1} is identified as the characteristic absorption peak of cobalt phthalocyanine. Characteristic absorption peaks of NH_2-MIL-101(Fe) at 768 cm^{-1} and 1658 cm^{-1} are attributed to the $-NH_2$ distorted vibration and $-NH_2$ variable angle vibration, respectively. Similarly, XRD spectra could confirm that Copc was successfully incorporated into NH_2-MIL-101(Fe) (Fig. 3b). Contact angle measurements confirm that the presence of the MOF@Copc layer achieves a better solid–liquid interface (Fig. 3c). As depicted in the SEM and TEM images, NH_2-MIL-101(Fe) exhibits a smooth surface with uniformly biconical-shaped blocks (Fig. 3d–e and Fig. S5 and S6, ESI†). Upon doping with Copc, the particles adhere to the surface of the MOF structure, which results in a roughened surface. Concurrently, the elemental distribution was analyzed using a transmission electron microscopy elemental map. NH_2-MIL-101(Fe)@CoPc displays elements such as C, N, O, Fe, and Co, well-distributed throughout the selected TEM image areas, indicating that Copc was successfully dispersed on the surface of NH_2-MIL-101(Fe). Finally, NH_2-MIL-101(Fe) exhibits a specific surface area of 172.62 $m^2\ g^{-1}$ (Fig. 3g), attributed to its larger surface area and porous structure. However, in the composite, the loaded Copc nanoparticles may obstruct the pores of NH_2-MIL-101(Fe), leading to a reduction in the nitrogen adsorption capacity of the NH_2-MIL-101(Fe)@CoPc nanocomposite, further proving that Copc was successfully loaded on the NH_2-MIL-101(Fe).

The enrichment effect of the MOF on $TFSI^-$ was demonstrated through molecular dynamics simulations (Fig. 4a and Fig. S7–S9, ESI†). The radial distribution function shows that under the action of the MOF structure, the distance of the $TFSI^-$ anion from the lithium surface typically ranges between 0.18 nm and 0.4 nm. The result is primarily attributed to the coordinated effects involving the Lewis acid–base interaction of the central ion Fe^{3+} and the hydrogen bond formed by the H atom in the amino group, which effectively secures the $TFSI^-$ anion closer to the lithium surface.[29–31] In the control group, the distance between the $TFSI^-$ anion and the lithium surface typically ranges from 0.24 nm to 0.8 nm, confirming that the strong repulsive force between the lithium metal and the anion pushes the anion away. The coordination numbers reveal that in the experimental MOF group, the coordination of $TFSI^-$ with the lithium surface is 0.42, compared to 0.13 in the control group. This suggests that the addition of MOF enables the lithium metal surface to more effectively absorb the $TFSI^-$, facilitates the decomposition of $TFSI^-$, and consequently boosts the formation of the LiF-SEI. To further demonstrate the enrichment effect of MOF on $TFSI^-$ anions, Li‖Li cells were

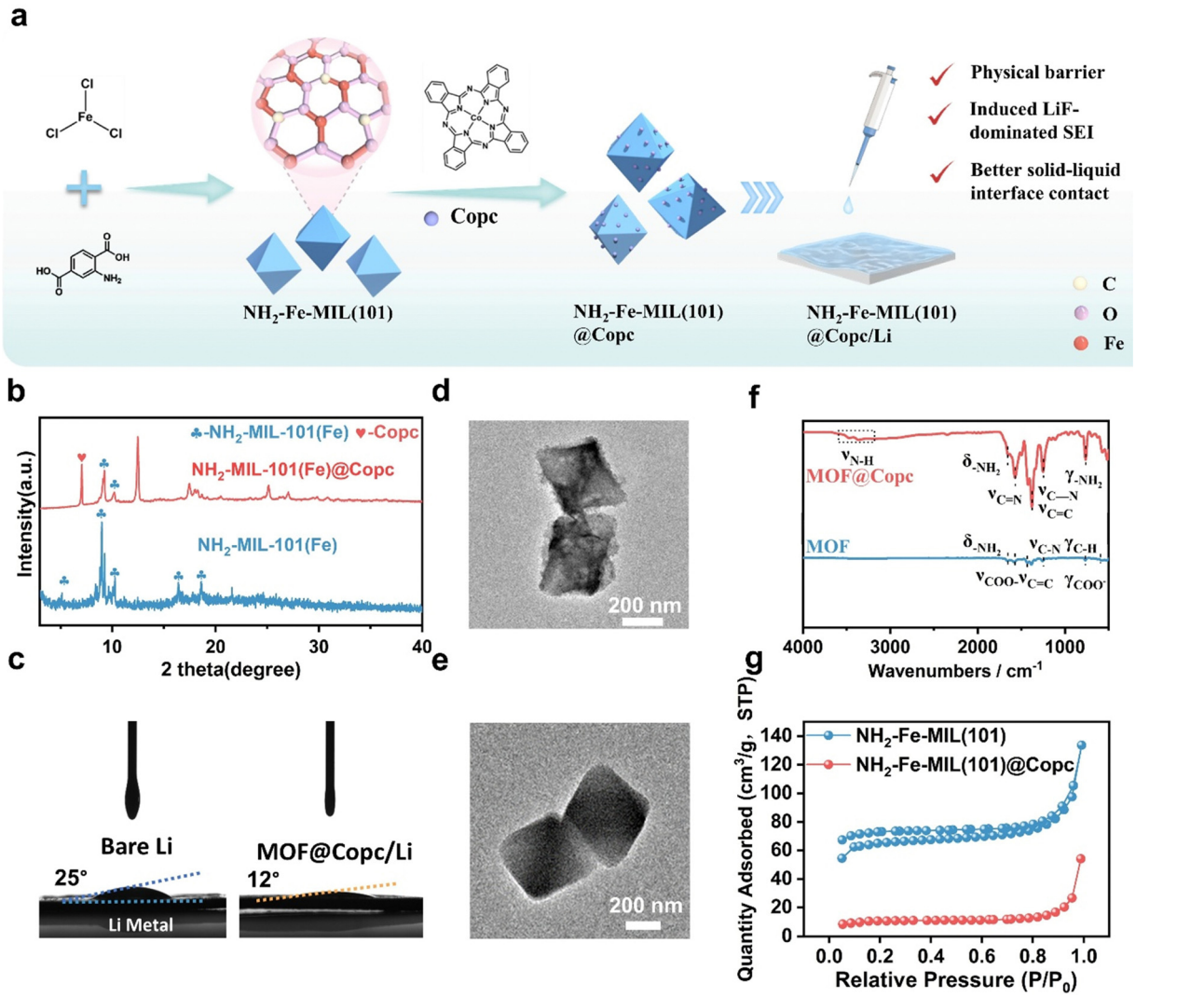

Fig. 3 Characterization of the composite NH_2-MIL-101(Fe)@Copc (a) schematic diagram of the preparation of NH_2-MIL-101(Fe) and NH_2-MIL-101(Fe)@CoPc nanocomposite. (b) XRD of NH_2-MIL-101 (Fe) and NH_2-MIL-101 (Fe)@CoPc. (c) Contact angle measurement of bare Li and MOF@-Copc/Li surfaces. (d) and (e) TEM image of NH_2-MIL-101(Fe) and NH_2-MIL-101(Fe)@CoPc. (f) FTIR spectra of NH_2-MIL-101(Fe)@CoPc. (g) N_2 adsorption–desorption isotherm.

assembled in the electrolytic cell for *in operando* Raman observations (Fig. 4d and e and Fig. S10, ESI†). The migration of $TFSI^-$ anions within electrolyte systems is evaluated by observing variations in anion strength between solid and liquid phases. After applying a constant current to the symmetric cell, $TFSI^-$ began to migrate, resulting in a gradual decrease in concentration on the upper side and an increase on the lower side. The presence of the modification layer mitigated the decrease in $TFSI^-$ concentration, limiting the movement of $TFSI^-$ and resulting in a slower decrease in concentration on the upper side. This provides strong support for the assertion that the modified MOF layer can enrich LiTFSI at the interface. Meanwhile, the red-shift phenomenon observed in both Raman and NMR spectra demonstrates that the MOF interacts with LiTFSI, leading to enrichment at the interface (Fig. 4b and c).

To verify the effect of the modification layer on the kinetics, the redox behavior of LiTFSI was examined using cyclic voltammetry (CV), revealing a distinct cathodic peak at approximately 1.2 V (Fig. S11, ESI†). The observed increase in peak intensity is correlated with an enhanced reduction reaction of $TFSI^-$. The substantial difference in peak intensities indicates that cobalt phthalocyanine fosters an electron-rich environment, thereby accelerating the reduction kinetics of $TFSI^-$. Additionally, a notable peak around 0.3 V corresponds to the low potential deposition of Li.[32] Around 1.6 V, the redox peak of $LiNO_3$ is observed, with the variation in peak intensities suggesting that the electron-rich environment also enhances the electron-driven decomposition reaction of $LiNO_3$.[33]

To elucidate the positive effects of the modification layer on SEI formation, X-ray photoelectron spectroscopy (XPS) was employed to analyze the composition of the SEIs after cycling. As shown in Fig. 4f, within the C 1s spectra, the content of product $-CF_2$ predominates, while that of reactant $-CF_3$ is significantly reduced. The positive effect of cobalt phthalocyanine on the

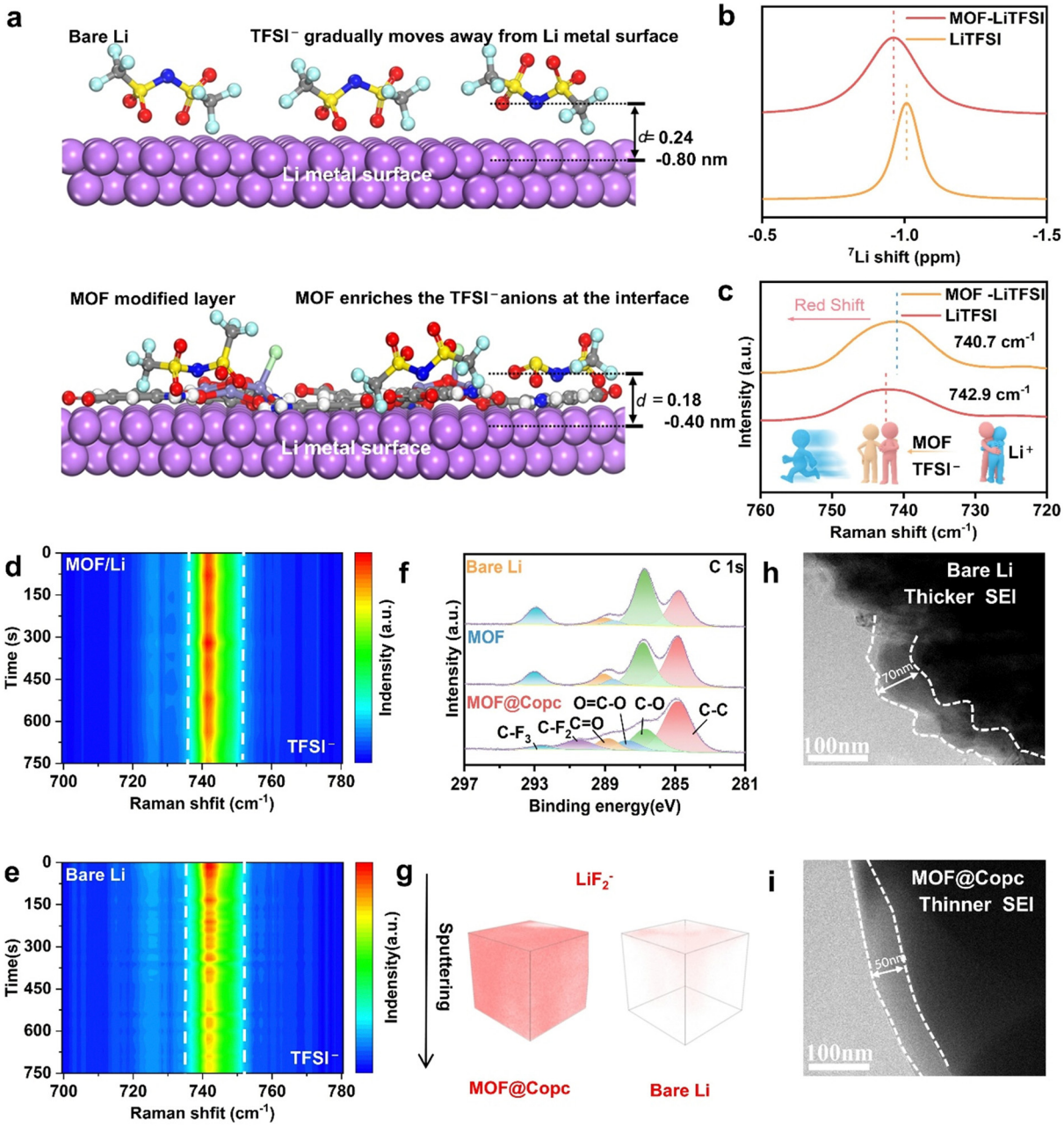

Fig. 4 Influence of MOF@Copc modified layer on SEI composition (a) schematic diagram of the distance between the $TFSI^-$ anion and the MOF/Li and Li surface. (b) and (c) The Raman and ^7Li NMR spectra of MOF-LiTFSI and LiTFSI. (d) and (e) *In operando* Raman patterns of $TFSI^-$ characteristic peaks in the Li‖Li system and the MOF/Li‖Li/MOF system. (f) XPS spectra of C 1s for bare Li, MOF/Li, and MOF@Copc/Li electrodes. (g) TOF-SIMS spectra of the lithium surface after cycling in a Li‖Li and MOF@Copc/Li‖Li/MOF@Copc battery. Here LiF_2^- signal is chosen to represent LiF. (h) and (i) Microstructure of SEI under cryo-electron microscopy.

electron transfer kinetics noticeably enhances the charge-induced decomposition reaction of LiTFSI. In the F 1s spectra, the MOF@Copc-modified layer yielded the highest LiF content (Fig. S12, ESI†). The same conclusion was reached through an analysis of the Li 1s data (Fig. S13, ESI†). At the same time, significant changes in Li_3N content were observed, stemming from the reaction of the $-NH_2$ group in the MOF with lithium metal,[34–36] and from electron-rich environments that facilitate the decomposition of $LiNO_3$. TOF-SIMS was utilized to analyze the differences in the distribution of LiF_2^-, LiF_3^-, and Li_2F^- ion fragments in SEI along the depth direction (Fig. 4g and Fig. S14, ESI†). The intensity of these fragments indicates that LiF produced by the modification layer is more uniformly distributed across the cross-section and vertical plane, completely exceeding the LiF content in the bare Li metal. The microstructure of the SEIs was examined using cryo-electron microscopy, revealing evident differences among the SEIs (Fig. 4h and i). The unmodified samples yielded a thick and inhomogeneous SEI, measuring

70 nm in thickness, whereas the modified samples formed a thin and homogeneous SEI with a thickness of just 50 nm. The thin and homogeneous SEI is crucial for regulating lithium deposition behavior and ion transport kinetics.[37,38]

To gain a deeper understanding of the significance of constructing MOF@Copc-ASEI, its electrochemical performance was assessed by assembling asymmetric Li–Cu half-cells. The MOF@Copc/Cu–Li cells exhibit satisfactory coulombic efficiency (CE) values and extended operating lives (Fig. 5a and Fig. S15, ESI†). Lithium modified with MOF@Copc/Li–Cu exhibits stable cycling for over 650 cycles at 1 mA cm^{-2} (1 mA h cm^{-2}), achieving an average coulombic efficiency (CE) value of 98.85%. The MOF@Copc/Li-modified battery sustains more than three times the number of cycles compared to the other two batteries. Moreover, the half-cell MOF@Copc/Cu–Li demonstrated notably impressive cycling stability, even when the current density was increased to 3.0 mA cm^{-2} (Fig. 5b). The superior electrochemical performance demonstrated that MOF@Copc-induced construction of LiF-rich SEI not only enhances the stable cycling characteristics of the cell but also improves coulombic efficiency. Additionally, the nucleation barrier of Li was investigated using the time–voltage test curve (Fig. 5c), MOF@Copc exhibited a low lithium nucleation overpotential of 59.7 mV at 3 mA cm^{-2}. However, the MOF/Cu–Li cells and bare Cu cells demonstrated high lithium nucleation overpotentials of 73.6 mV and 117.4 mV, respectively. The lowest nucleation and plateau overpotentials suggest that the ASEI-induced LiF interface effectively reduces the energy barrier to lithium nucleation and growth.[12,39] To investigate the impact of the modified layer on Li-ion transfer kinetics, Li‖Cu half-cells and Li‖Li symmetric cells were assembled for subsequent measurements (Fig. S16, ESI†). Notably, the MOF@Copc-modified symmetric cell exhibits an exceptionally high Li^+ transfer number (t_{Li^+}) of 0.765, compared

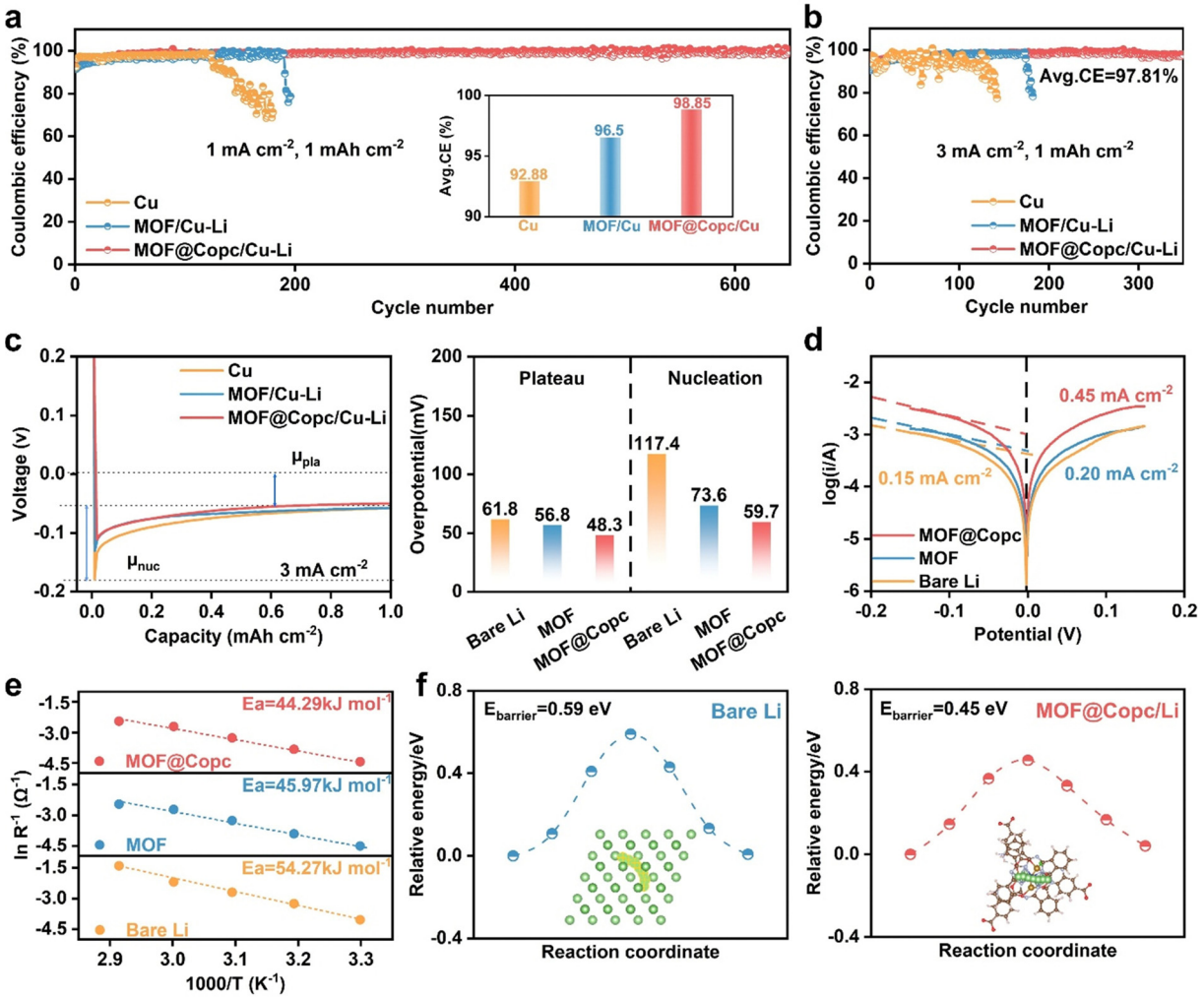

Fig. 5 Electrochemical transport kinetics of modified lithium metal anodes (a) coulombic efficiencies of Li–Cu, MOF/Li–Cu, and MOF@Copc/Li–Cu cells at 1 mA cm^{-2} with a capacity of 1 mA h cm^{-2}. (b) Coulombic efficiencies of Li–Cu, MOF/Li–Cu, and MOF@Copc/Li–Cu cells at 3 mA cm^{-2} with a capacity of 1 mA h cm^{-2}. (c) The voltage–capacity curves of Li–Cu, MOF/Li–Cu, and MOF@Copc/Li–Cu cells at 3 mA cm^{-2} with a capacity of 1 mA h cm^{-2}. (d) Tafel curves of symmetric cells. (e) Effect of temperature on the interfacial impedances of the modified and unmodified anode. (f) Li^+ diffusion pathway and corresponding energy barriers of bare Li and MOF@Copc/Li.

to that of bare lithium. Higher t_{Li^+} is achieved by anion immobilization.[40] The Tafel curves indicate that the exchange current density, enhanced by MOF@Copc (I_0 = 0.45 mA cm^{-2}), is three times that of the unmodified one (I_0 = 0.15 mA cm^{-2}) (Fig. 5d). This enhancement suggests that the MOF@Copc modification layer significantly improves Li^+ diffusion processes, thereby accelerating interfacial transfer kinetics.[41] To further explore the effect of the MOF@Copc protective layer on ion transport, the activation energy (E_a) for lithium-ion migration at the interface was determined using the Arrhenius equation (Fig. 5e and Fig. S17, ESI†). The results indicated that bare Li (54.27 kJ mol^{-1}) > MOF (45.97 kJ mol^{-1}) > MOF@Copc (44.29 kJ mol^{-1}). The spontaneous synergistic optimization strategy facilitates the enrichment and decomposition of $TFSI^-$, resulting in the formation of a LiF-rich SEI that substantially enhances Li^+ transport kinetics.[42,43] Simulation results of the lithium-ion migration path reveal that the MOF@Copc interface layer displays a reduced lithium-ion diffusion barrier, promoting the rapid and uniform transport of Li ions (Fig. 5f)

To demonstrate the enhanced cycling stability of MOF@Copc modification for lithium metal batteries (LMB), constant-current charge/discharge tests were conducted on symmetric cells (Fig. 6a). At a current density of 1 mA cm^{-2}, bare Li cells experienced a sharp increase in overvoltage after just five cycles. For the MOF/Li symmetric cell, the voltage abruptly increased after 1000 hours. In contrast, the MOF@Copc-modified symmetric cell maintained continuous operation for 2000 hours. The amplified voltage curve illustrates that the MOF@Copc/Li batteries maintain a stable voltage plateau throughout the plating/stripping process.

To visualize the precise regulatory effect of the MOF@Copc layer on the excellent interface, the lithium electrode morphology of Li‖Li symmetric batteries after 1 mA cm^{-2} constant-current charging and discharging was examined using atomic force microscopy (AFM) (Fig. 6b). The surface roughness of the unmodified lithium anode, which measured 279.9 nm, is primarily attributable to the formation of numerous lithium dendrites and dead lithium after 100 cycles. The surface of the

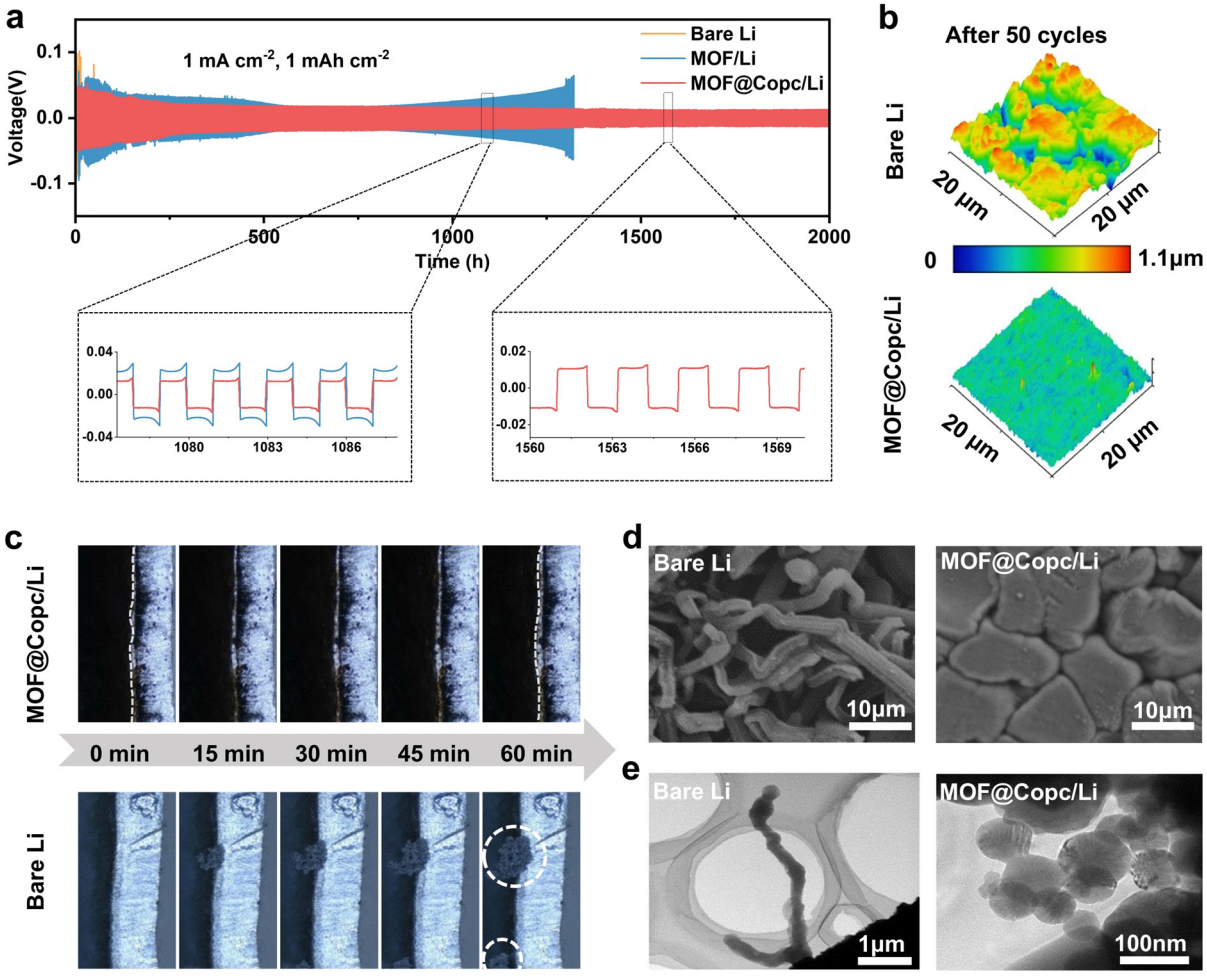

Fig. 6 Electrochemical performance and characterization of lithium deposition layer (a) current density of 1 mA cm^{-2} with a capacity of 1 mA h cm^{-2}. (b) The atomic force microscopy (AFM) testing of the surface roughness of lithium electrodes after cycling. (c) *In situ* optical microscopy observations of the Li deposition/stripping process on bare Li foil and MOF@Copc/Li. (d) Corresponding SEM images after plating for bare Li and MOF@Copc/Li. (e) Cryo-electron microscopic observation of the morphology of lithium deposition.

MOF@Copc-modified electrode remains smooth, with a roughness of 494.3 pm, which is mainly attributed to the fact that LiF plays an important role in inhibiting dendrite growth and promoting uniform deposition of lithium. Additionally, *in operando* optical microscopy (OM) was employed to observe Li plating behavior in real time. As shown in Fig. 6c and Fig. S18 (ESI†), both the bare Li and MOF@Copc/Li anodes exhibited smooth surfaces before lithium plating began. Subsequently, uneven Li plating emerged on the surface of bare Li after 15 minutes, leading to the formation of numerous lithium dendrites. In contrast, the MOF@Copc/Li anode gradually thickens during the entire lithium plating process while consistently maintaining a uniform and smooth surface. These results illustrate that the MOF@Copc/Li anode effectively inhibits the growth of lithium dendrites throughout the cycling process.

To more effectively demonstrate the morphological modulation of lithium deposition by the MOF@Copc protective layer during the cycling process, the morphological evolution during lithium deposition/exfoliation was investigated using non-*in situ* scanning electron microscopy (Fig. 6d and Fig. S19 and S20, ESI†). At a current density of 1 mA cm^{-2} and capacity of 1 mA h cm^{-2}, numerous mossy lithium dendrites appeared on the surface of the bare lithium electrode, exhibiting a sparse and discrete deposition morphology. For the MOF/Li anode, the deposited lithium displayed a non-dense morphology with visible cracks. In contrast, the surface of the MOF@Copc-modified electrode exhibits a smooth and dense bulk deposition morphology. Further analysis of SEM images at the higher current density and capacity following the fiftieth cycle shows that MOF@Copc/Li exhibits uniform and flat lithium deposition morphology, which suggests that the formation of LiF-rich SEI induced by the protective layer of MOF@Copc can significantly inhibit the dendrites and improve the stability of the interface.[44] Meanwhile, satisfactory spherical lithium deposition is more

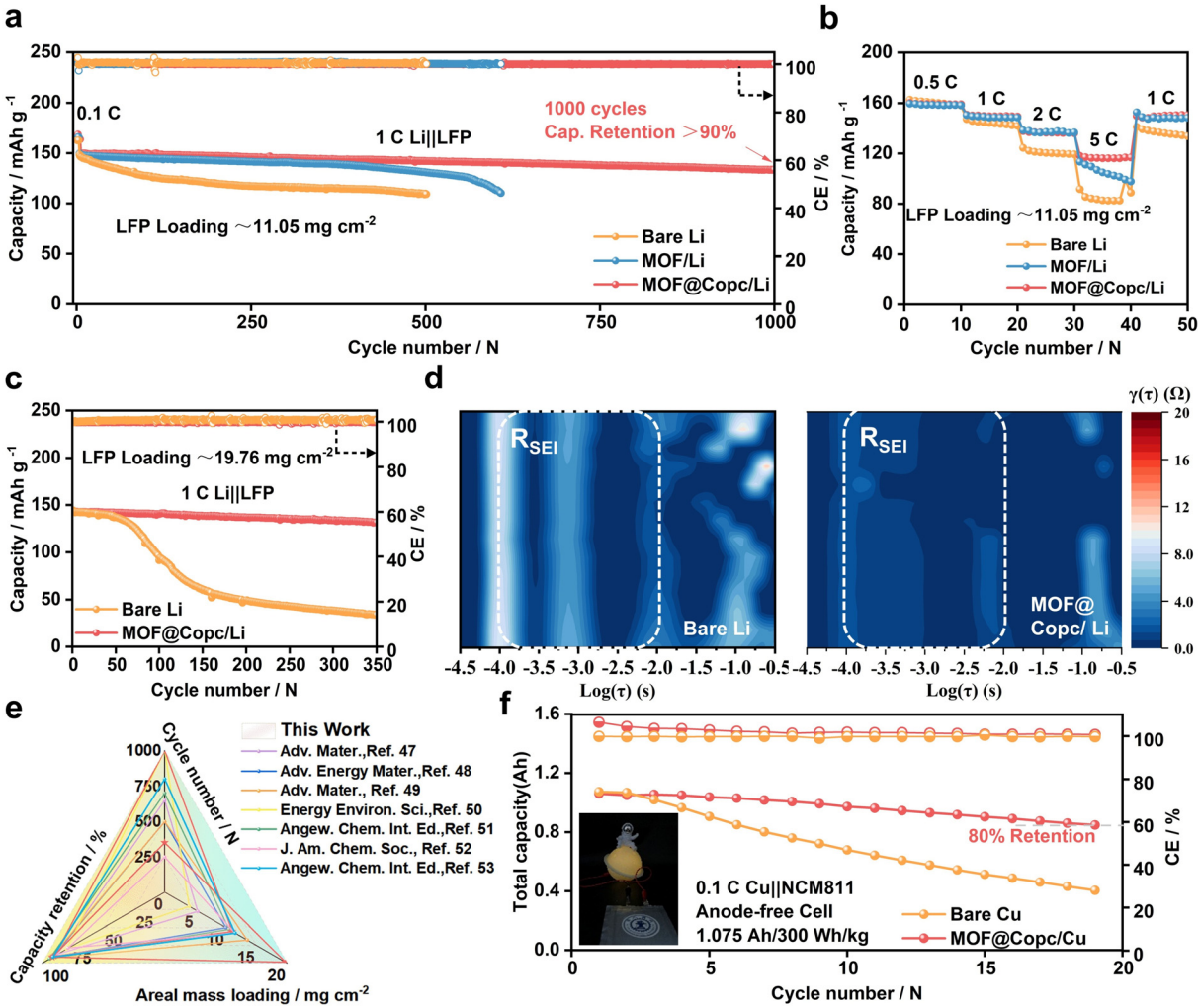

Fig. 7 Battery performance of MOF@Copc protective layer (a) cycling performance of LFP-MOF@Copc/Li, LFP-MOF/Li, and LFP-bare Li cells at 1C rate. (b) Rate performance of LFP-MOF@Copc/Li, LFP-MOF/Li, and LFP-bare Li cells at 0.5C, 1C, 2C, 5C. (c) Cycling performances of high-loading LFP-MOF@Copc/Li and bare Li cells at 1C rate. (d) Distribution of relaxation times (DRT) results of LFP‖bare Li and LFP‖MOF@Copc/Li cells in the voltage range of 3.5–4.2 V. (e) Comparison of electrochemical performance of lithium metal anode modified by MOF@Copc with related work. (f) Cycling performance of the Cu‖NCM811 and MOF@Copc/Cu ‖ NCM811 pouch-type cell at 0.1C, Tests to light up commercially available mini-lamps.

readily observable using cryo-electron microscopy (Fig. 6e and Fig. S21, ESI†). Owing to the minimal volume of the spherical units, the probability of interfacial side reactions in lithium metal is minimized, thereby enhancing the cycling reversibility of lithium metal batteries.[45,46]

A typical full cell was assembled to further explore the practical application potential of the MOF@Copc layer. The lithium metal anode, featuring a MOF@Copc-modified layer, was initially paired with an LFP cathode at a loading of 11.05 mg cm^{-2} (Fig. 7a). After enduring 1000 cycles, the cell demonstrated remarkable stability, with a capacity retention rate exceeding 90%. The electrochemical performance of MOF@Copc is notably superior compared to that reported in much of the existing literature (Fig. 7e).[47–53] Meanwhile, under high current density (3C), the modified lithium anode maintains a capacity retention of up to 97.58% after 600 cycles (Fig. S22, ESI†). Surprisingly, the cell performance also remains outstanding when paired with higher loadings of LFP (Fig. 7c). Therefore, *in situ* electrochemical impedance spectroscopy (EIS) measurements and relaxation time distribution (DRT) of LFP‖Li cells were utilized for analysis (Fig. 7d and Fig. S23, ESI†). The change in the integrated area of the peak features associated with interfacial resistance after 100 cycles was significantly smaller for MOF@Copc/Li than for the cells with unmodified bare Li. The outcome is primarily attributed to the enhanced cycling stability resulting from an improved interface by the artificial SEI.[54]

To further verify the rate capability of the full battery, charge–discharge rate tests were conducted at various current densities. As the charge–discharge current density increased, the discharge capacity of the battery was also increased to (0.5, 1, 2, and 5C, corresponding to 162.65, 149.81, 137.71, and 118.05 mA h g^{-1}, respectively) (Fig. 7b). When the current density returned to 1C, a capacity of 149.57 mA h g^{-1} could be restored, exhibiting a satisfactory high magnification tolerance. Particularly at a current density of 5C, the capacity of MOF@Copc/Li was found to be 1.4 times that of bare lithium metal batteries. Voltage distribution diagrams at various rates demonstrate that, compared with LFP/bare Li cells, MOF@Copc/Li exhibits reduced voltage polarization (Fig. S24, ESI†). The MOF@Copc/Li cell exhibits excellent long-term cycling stability at a high rate of 20C, equivalent to one cycle every three minutes (Fig. S25, ESI†). After more than 9000 cycles, the capacity retention rate achieved an impressive 95.18%. The electrochemical cycling stability is attributed to the advanced spontaneous cascade optimization strategy. The synergistic effect of anion enrichment and excellent anion decomposition kinetics contributes to the SEI with a predominantly inorganic composition, which effectively regulates Li^+ diffusion kinetics and lithium deposition behavior, facilitating fast charging of lithium-metal batteries.[55]

Subsequently, we further explore the compatibility of the modified MOF@Copc layer with high-voltage cathodes, we employed a high-loading $LiNi_{0.8}Co_{0.1}Mn_{0.1}O_2$ (NCM811) cathode (Fig. S26, ESI†). The cycling stability of MOF@Copc-modified layer batteries demonstrates that the proportion of inorganic components in the induced SEI is directly proportional to the cycle life of lithium metal batteries (LMB). The rate performance of MOF@Copc/Li-modified full cells is significantly superior to that of both bare Li and MOF/Li cells, particularly at high current densities (Fig. S27, ESI†). To achieve higher energy density, cycle stability tests were conducted under more challenging commercial pouch cell conditions. Notably, MOF@Copc/Cu demonstrates a longer cycle life compared to the unmodified copper foil. These pouch batteries are capable of powering light bulbs, thereby demonstrating their commercial potential in the field of flexible wearable electronics (Fig. 7f and Fig. S28, ESI†).

Conclusions

In summary, we propose the spontaneous cascade optimization strategy to modulate inorganic-rich SEIs. This strategy is used to achieve a two-step optimization by first enriching the anions at the interface and then modulating the electron transfer kinetics to promote the oxidative decomposition of the anions. Simulations and characterization studies reveal the critical role of Copc in the decomposition kinetics, and the electron-directed conduction of the electron-rich structure significantly lowers the decomposition energy barriers, thereby facilitating the decomposition of C–F bonds. It was demonstrated through *in operando* Raman spectroscopy and molecular dynamics simulations that NH_2-MIL-101 (Fe) enriches anions at the interface. Therefore, the synergistic effect of these two composites, facilitated by the spontaneous cascade optimization strategy, maximizes the decomposition of anions. *In situ* construction of LiF-rich SEIs modulates Li^+ transport kinetics and facilitates uniform lithium deposition, thereby resulting in excellent electrochemical performance of the modified anode. Notably, the MOF@Copc-modified Li‖Cu cell exhibited an exceptionally long cycle life. When paired with a highly loaded LFP, the performance exceeds that documented in the existing literature. Meanwhile, pouch batteries exhibit excellent electrochemical performance at 0.1C. We anticipate that the successful application of MOF@Copc ASEI will offer innovative insights to achieve uniform lithium deposition and enhance stable long-lifespan performance.

Experimental section

Preparation of NH_2-MIL-101(Fe)

As for the preparation of NH_2-MIL-101(Fe), 2.75 g of $FeCl_3 \cdot 6H_2O$ and 1.105 g of 2-aminoterephthalic acid were each dissolved separately in 40 mL of DMF to prepare solution A and solution B. The two solutions were treated with ultrasonic for 15 min. Next, solution B was gradually added to solution A under ultrasonic to obtain a homogeneous solution. The mixture was then transferred to the Teflon-lined autoclave and heated at 110 °C for 24 h. After the product was cooled to room temperature, it was collected by centrifugation at 10 000 rpm for 5 minutes, followed by washing with DMF three times and

ethanol twice. The product was then dried under vacuum at 60 °C for 12 hours. Finally, NH_2-MIL-101(Fe) powder was obtained by grinding.[56]

Preparation of NH_2-MIL-101(Fe)@Copc

NH_2-MIL-101(Fe)@CoPc composites were synthesized *via* the impregnation method. 5 mg of CoPc was weighed and transferred into a 50 mL single-necked flask, followed by the addition of 40 mL of DMF to ultrasonically dissolve the CoPc. 60 mg of NH_2-MIL-101(Fe) was then added, and the mixture was macerated at 75 °C for 40 hours. The solvent was removed by distillation under reduced pressure. The residue was washed by centrifugation with ethanol several times and then dried at 120 °C for 12 hours. The reagents used during the experiment were Macklin reagents.

Preparation of NH_2-MIL-101(Fe)@Copc/Li

60 mg of MOF@Copc powder was dissolved in 1.64 mL of tetrahydrofuran and stirred for 4 hours. Subsequently, in the glove box, 50 μL of the solution was dropped on lithium tablets and dried for 2 hours to obtain MOF@Copc/Li.

Electrode preparation and battery assembly

The cathode, Li metal anode, PP battery separator, and 40 μL electrolyte were assembled into a CR2025 button cell. All the CR2025 coin cells above and the pouch battery were assembled in an argon-filled glove box with oxygen content <0.1 ppm and H_2O content <0.1 ppm.

Battery testing

The cycling stability of Li‖Li, Li‖Cu, Li‖Li, and pouch cell were conducted using the Neware multichannel battery testing systems at 30 °C. The cycle performance of $LiFePO_4$‖Li batteries are tested between 2.5 and 4.2 V (1.0 M LiTFSI in dioxolane (DOL)/1,2-dimethoxyethane (DME) = 1 : 1 (v/v) with 2.0% $LiNO_3$, Duo Duo chem), while NCM811‖Li batteries were tested at charge–discharge ranges of 2.8–4.3 V. (1 M $LiPF_6$ in DEC : EC = 1 : 1 vol% with 10%FEC, Duo Duo chem). The NCM811‖Cu anode-free lithium-metal pouch batteries were tested at charge–discharge ranges of 2.75–4.2 V. (1 M $LiPF_6$ in DEC : EC = 1 : 1 Vol% with 10%FEC, Duo Duo chem). The C rates in all of the electrochemical measurements are defined based on 1C = 200 mA g^{-1} (NCM811) and 1C = 170 mA g^{-1} ($LiFePO_4$). LFP, PVDF, and CB were mixed by ball milling in NMP in a mass ratio of 8 : 1 : 1, then made into a slurry, uniformly coated onto charcoal-coated aluminum foil, and dried in a vacuum oven at 120 °C for 12 hours. The mass loading of the active substance was about 2.1 mg cm^{-2}.

Materials characterization

The Fourier transform infrared (FT-IR) spectra were tested on a Thermo Nicolet iS50 Fourier infrared spectrometer. The material MOF@Copc was determined using X-ray diffractometer (XRD, Bruker D8 ADVANCE). The SEM images were conducted by field-emission scanning electron microscopy (FESEM, Carl Zeiss Gemini 500), EDX spectroscope attached to SEM (EDX mapping). Atomic force microscope (AFM, Bruker Dimension ICON) was employed to observe surface morphology. Nuclear magnetic resonance (NMR) spectra were tested on a JEOL JNM-ECZ400S/L1 NMR spectrometer with d6-DMSO as solvent. The Raman spectroscopy measurement was performed using a Laser Raman Spectrometer (InVia Qontor, Renishaw) with a 785 nm excitation wavelength. X-ray photoelectron spectrometer (XPS, Thermo Fisher ESCALAB Xi^+) was used to conduct surface elemental analysis. Time-of-flight secondary ion mass spectrometry (TOF-SIMS) analysis was performed using a PHI nano TOF‖time-of-flight SIMS equipped with a 30 kV Bi-cluster liquid metal ion gun. Cryo-transmission electron microscopy (Cryo-TEM) characterization was performed on a 200 kV F FEI Talos F200C. Changes in morphology of the Li electrode during the electrochemical deposition process were directly observed by using an *in situ* optical microscope. The surface topography of the lithium after the cycle was observed using a Laser confocal microscopy (CLSM, Leica DCM8).

Electrochemical measurements

Redox reactions on electrode surfaces. The electrochemical processes were described using cyclic voltammetry (CV) and the reaction kinetics were investigated using a Cu‖Li asymmetric cell with a scan rate of 0.0005 V s^{-1} over the voltage range of 0 V to 2.5 V.

Lithium-ion transference number. The Li^+ transference number (t_{Li^+}) of the electrolyte was measured through the chronoamperometry method with a typical Li‖Li symmetric cell. The t_{Li^+} can be calculated by the following equation:

$$t_{Li^+} = \frac{I_s(\Delta V - I_0 R_{i0})}{I_0(\Delta V - I_s R_{is})} \quad (1)$$

where ΔV is the DC polarization voltage (10 mV), I_0 and I_s are individually the initial and steady-state current of the symmetric cell before and after polarization. At the same time, R_{i0} and R_{is} are the interfacial resistances of the symmetric cell before and after polarization, respectively.

Exchange current density. The Tafel plot parameters of a symmetric lithium battery were tested from −0.25 V to 0.25 V at a scan rate of 1 mV s^{-1}, and the exchange current density was evaluated according to the Tafel equation:

$$\eta = -\left(\frac{2.303RT}{\alpha F}\right)\log i_0 + \left(\frac{2.303RT}{\alpha F}\right)\log i \quad (2)$$

where i is the current density, η is the overpotential, and α is the transfer coefficient. The Tafel curve represents the logarithm of the current density *versus* the overpotential. Using the extrapolation method, on the linear Tafel region, the intercept with the Y-axis at the overpotential of 0 represents the exchange current density.

Desolvation energy. To measure the desolvation energy (E_a) of electrolytes, temperature-dependent EIS measurements of a Li‖Li symmetric cell were conducted over a frequency range from 10^6 Hz to 0.1 Hz using a CHI660E at various temperatures. The E_a value was obtained by fitting the data into the equation:

$$R_{CT}^{-1} = A\exp(-E_a/RT) \quad (3)$$

where T is the absolute temperature, R_{CT} is desolvation resistance, A is the pre-exponential constant, E_a is the activation energy of desolvation, and R is the standard gas constant.

Calculation methods

DFT calculation. The first-principle-based geometry optimization calculations were carried out within density-functional theory (DFT), implemented in the Vienna *ab initio* simulation package (VASP) code,[57] using the frozen-core projector augmented-wave (PAW) method[58] to describe the interaction between the atomic cores and the valence electron density. The exchange–correlation potential was approximated within the generalized gradient approximation (GGA) using the Perdew–Burke–Ernzerhof (PBE) functional[57] which was used to calculate electron–electron exchange and correlation interactions. A kinetic energy cutoff of 400 eV was chosen to ensure complete convergence. The Brillouin zone was sampled with the k-grid of $1 \times 1 \times 1$. The conjugate gradient (CG) method was used for structural relaxation, simultaneously minimizing total energy and interatomic forces. The convergence tolerance for the total energy was set at 10^{-5} eV, and the residual force on each atom was limited to less than 0.05 eV Å^{-1}. Additionally, dispersion-corrected DFT-D_3 schemes were employed to account for van der Waals interaction.[59]

The adsorption energy (E_{ads}) can be calculated as follows:

$$E_{ads}(Li^+ - TFSI^-) = E(Li^+ - TFSI^-) - E(Li^+) - E(TFSI^-) \quad (4)$$

$$E_{ads}(MOF - TFSI^-) = E(MOF - TFSI^-) - E(MOF) - E(TFSI^-) \quad (5)$$

$$E_{ads}(MOF - Copc) = E(MOF - Copc) - E(MOF) - E(Copc) \quad (6)$$

where $E(Li^+ - TFSI^-)$ is the energy of $Li^+ - TFSI^-$, $E(Li^+)$ is the energy of Li atom, $E(TFSI^-)$ is the energy of $TFSI^-$, $E(MOF - TFSI^-)$ is the energy of $MOF - TFSI^-$, $E(MOF - Copc)$ is the energy of $MOF - Copc$, $E(Copc)$ is the energy of Copc.

MD simulation. The distance between $TFSI^-$ and lithium surface was studied by molecular dynamics (MD) simulation. Using the Forcite module in Materials Studio, the $TFSI^-$ and lithium metal interface were calculated under the universal force field (UFF). The dimension length of the electrode on the xoy plane is 28.22 A × 28.22 A. The simulation added 2 layers of lithium metal, 100 Li^+ and 100 $TFSI^-$ anions. All Li^+ ions and $TFSI^-$ are randomly loaded into the rectangular box. When optimizing, the lithium metal interface layer and the MOF layer are fixed, so that all Li^+ and $TFSI^-$ anions can move freely. After the geometric optimization of the structure, a molecular dynamics simulation was carried out. The MD calculations were all carried out in the NVT system (T = 298.0 K) with a time step of 1 fs and a total simulation time of 3000 ps. The van der Waals and Coulomb interactions are considered by atom-based and Ewald methods, respectively, with a cut-off value of 12.5 A. The equation of motion is integrated with a time step of 1 fs. Output dynamic trajectories of the system every 5 ps. The distance from the $TFSI^-$ anion to the surface layer is obtained by RDF. The overall simulation time was long enough to ensure that the system was in equilibrium.

Author contributions

F. Z. and H. L. and Y. W. contributed equally to this work, performed the experiments, and co-wrote the paper. X. Z., Y. C., and Y. Z. conceived the idea, planned the study, designed the experiment, and analyzed the data. F. Z. performed all of the experiments with the assistance of X. Y., H. W., and S. D. W. Y., and X. C. directed the revision of the article. All of the authors reviewed and commented on the manuscript.

Data availability

All datasets generated or analyzed during the current study are included in the paper and its ESI.†

Conflicts of interest

The authors declare no conflict of interest.

Acknowledgements

This work was supported by the Key Research and Development Program of Shaanxi Province (2024PT-ZCK-82), and the Basic Strengthening Program (2022-JCJQ-JJ-0278). The Instrumental Analysis Center of Xi'an Jiaotong University is acknowledged for providing the test service. The authors deeply acknowledge the teachers at the Instrumental Analysis Center of Xi'an Jiaotong University, including Ms Jiamei Liu for the assistance with XPS, Ms Jia Liu for the assistance with *in situ* Raman test, and Ms Yan Liang for the assistance with the TOF-SIMS test.

References

1 H. Chen, Y. F. Yang, D. T. Boyle, Y. K. Jeong, R. Xu, L. S. de Vasconcelos, Z. J. Huang, H. S. Wang, H. X. Wang, W. X. Huang, H. Q. Li, J. Y. Wang, H. K. Gu, R. Matsumoto, K. Motohashi, Y. Nakayama, K. J. Zhao and Y. Cui, *Nat. Energy*, 2021, **6**, 790–798.

2 X. He, D. Bresser, S. Passerini, F. Baakes, U. Krewer, J. Lopez, C. T. Mallia, Y. Shao-Horn, I. Cekic-Laskovic, S. Wiemers-Meyer, F. A. Soto, V. Ponce, J. M. Seminario, P. B. Balbuena, H. Jia, W. Xu, Y. B. Xu, C. M. Wang, B. Horstmann, R. Amine, C. C. Su, J. Y. Shi, K. Amine, M. Winter, A. Latz and R. Kostecki, *Nat. Rev. Mater.*, 2021, **6**, 1036–1052.

3 Y. Zhang, R. Qiao, Q. Nie, P. Zhao, Y. Li, Y. Hong, S. Chen, C. Li, B. Sun, H. Fan, J. Deng, J. Xie, F. Liu and J. Song, *Nat. Commun.*, 2024, **15**, 4454.

4 Z. J. Wang, Y. Y. Wang, Z. H. Zhang, X. W. Chen, W. Lie, Y. B. He, Z. Zhou, G. L. Xia and Z. P. Guo, *Adv. Funct. Mater.*, 2020, **30**, 2002414.
5 S. Y. Pan, J. W. Han, Y. Q. Wang, Z. S. Li, F. Q. Chen, Y. Guo, Z. S. Han, K. F. Xiao, Z. C. Yu, M. Y. Yu, S. C. Wu, D. W. Wang and Q. H. Yang, *Adv. Mater.*, 2022, **34**, 2203617.
6 Y. P. Gu, J. L. Hu, M. Lei, W. B. Li and C. L. Li, *Adv. Energy Mater.*, 2024, **14**, 2302174.
7 Y. P. Jiang, Q. Lv, C. Y. Bao, B. Wang, P. H. Ren, H. Y. Zhong, Y. Yang, X. M. Liu, Y. C. Dong, F. Jin, D. A. L. Wang, T. Xiong, H. K. Liu, S. X. Dou, J. Wang and J. M. Xue, *Cell Rep. Phys. Sci.*, 2022, **3**, 100785.
8 Y. Q. Liao, H. Y. Zhang, Y. F. Peng, Y. G. Hu, J. D. Liang, Z. L. Gong, Y. M. Wei and Y. Yang, *Adv. Energy Mater.*, 2024, **14**, 2304295.
9 X. Shen, R. Zhang, X. Chen, X. B. Cheng, X. Y. Li and Q. Zhang, *Adv. Energy Mater.*, 2020, **10**, 1903645.
10 P. B. Zhai, T. S. Wang, H. N. Jiang, J. Y. Wan, Y. Wei, L. Wang, W. Liu, Q. Chen, W. W. Yang, Y. Cui and Y. J. Gong, *Adv. Mater.*, 2021, **33**, 2006247.
11 Q. K. Zhang, X. Q. Zhang, J. Wan, N. Yao, T. L. Song, J. Xie, L. P. Hou, M. Y. Zhou, X. Chen, B. Q. Li, R. Wen, H. J. Peng, Q. Zhang and J. Q. Huang, *Nat. Energy*, 2023, **8**, 725–735.
12 S. Z. Chang, J. B. Fang, K. Liu, Z. H. Shen, L. Zhu, X. Jin, X. J. Zhang, C. Q. Hu, H. G. Zhang and A. D. Li, *Adv. Energy Mater.*, 2023, **13**, 2204002.
13 Y. Z. Yang, J. Wang, Z. L. Li, Z. Yang, B. Wang and H. L. Zhao, *ACS Nano*, 2024, **18**, 7666–7676.
14 H. Zhang, Z. Q. Zeng, F. F. Ma, X. L. Wang, Y. K. Wu, M. C. Liu, R. J. He, S. J. Cheng and J. Xie, *Adv. Funct. Mater.*, 2023, **33**, 2212000.
15 C. C. Su, M. N. He, M. Cai, J. Y. Shi, R. Amine, N. D. Rago, J. C. Guo, T. Rojas, A. T. Ngo and K. Amine, *Nano Energy*, 2022, **92**, 106720.
16 H. K. Bergstrom and B. D. McCloskey, *ACS Energy Lett.*, 2024, **9**, 373–380.
17 C. Q. Jin, A. Xiang, Z. X. Wang, Q. Q. He, B. X. Li, X. K. Zhang, Y. Xiang, P. B. Zhai and Y. J. Gong, *Adv. Energy Mater.*, 2025, **15**, 2402811.
18 P. Zhao, Y. Zhang, B. Sun, R. Qiao, C. Li, P. Hai, Y. Wang, F. Liu and J. Song, *Angew. Chem., Int. Ed.*, 2024, **63**, e202317016.
19 Z. Li, L. Wang, X. D. Huang and X. M. He, *Adv. Funct. Mater.*, 2024, **34**, 2408319.
20 Y. J. Liu, X. Y. Tao, Y. Wang, C. Jiang, C. Ma, O. W. Sheng, G. X. Lu and X. W. Lou, *Science*, 2022, **375**, 739–745.
21 Z. K. Ma, J. W. Chen, J. Vatamanu, O. Borodin, D. Bedrov, X. G. Zhou, W. G. Zhang, W. S. Li, K. Xu and L. D. Xing, *Energy Storage Mater.*, 2022, **45**, 903–910.
22 H. A. Wang, H. Cheng, D. G. Li, F. Q. Li, Y. Wei, K. Huang, B. W. Jiang, H. H. Xu and Y. H. Huang, *Adv. Energy Mater.*, 2023, **13**, 2204425.
23 S. S. Yan, F. X. Liu, Y. Ou, H. Y. Zhou, Y. Lu, W. H. Hou, Q. B. Cao, H. Liu, P. Zhou and K. Liu, *ACS Nano*, 2023, **17**, 19398–19409.
24 H. F. Zhuang, H. Xiao, T. F. Zhang, F. C. Zhang, P. Y. Han, M. Y. Xu, W. J. Dai, J. R. Jiao, L. Jiang and Q. M. Gao, *Angew. Chem., Int. Ed.*, 2024, **63**, e202407315.
25 X. Y. Zhou, F. F. Huang, X. D. Zhang, B. Zhang, Y. J. Cui, Z. H. Wang, Q. Yang, Z. S. Ma and J. Liu, *Angew. Chem., Int. Ed.*, 2024, **63**, e202401576.
26 W. Z. Liang, X. Y. Zhou, B. Zhang, Z. S. Zhao, X. Song, K. Chen, L. Wang, Z. S. Ma and J. Liu, *Angew. Chem., Int. Ed.*, 2024, **63**, e202320149.
27 J. Liu, D. W. Kang, Y. J. Fan, G. T. Nash, X. M. Jiang, R. R. Weichselbaum and W. B. Lin, *J. Am. Chem. Soc.*, 2023, **146**, 849–857.
28 Y. B. Song, S. Y. Hu, D. R. Cai, J. R. Xiao, S. F. Zhou and G. W. Zhan, *ACS Appl. Mater. Interfaces*, 2022, **14**, 9151–9160.
29 L. Wei, X. Xu, K. Xi, Y. Lei, X. Cheng, X. B. Shi, H. H. Wu and Y. F. Gao, *ACS Appl. Mater. Interfaces*, 2024, **16**, 33578–33589.
30 Y. H. Nie, T. Z. Yang, D. Luo, Y. Z. Liu, Q. Y. Ma, L. X. Yang, Y. Z. Yao, R. Huang, Z. Y. Li, E. M. Akinoglu, G. B. Wen, B. H. Ren, N. Zhu, M. Li, H. Liao, L. C. Tan, X. Wang and Z. W. Chen, *Adv. Energy Mater.*, 2023, **13**, 2204218.
31 L. Tu, Z. J. Zhang, Z. L. Zhao, X. Y. Xiang, B. H. Deng, D. Liu, D. Y. Qu, H. L. Tang, J. S. Li and J. P. Liu, *Angew. Chem., Int. Ed.*, 2023, **62**, e202306325.
32 C. Jiang, Q. Q. Jia, M. Tang, K. Fan, Y. Chen, M. X. Sun, S. F. Xu, Y. C. Wu, C. Y. Zhang, J. Ma, C. L. Wang and W. P. Hu, *Angew. Chem., Int. Ed.*, 2021, **60**, 10871–10879.
33 Q. C. Zhang, L. Xu, X. Y. Yue, J. J. Liu, X. Wang, X. Y. He, Z. D. Shi, S. Z. Niu, W. Gao, C. Cheng and Z. Liang, *Adv. Energy Mater.*, 2023, **13**, 2302620.
34 Z. Y. Han, H. R. Ren, Z. J. Huang, Y. B. Zhang, S. C. Gu, C. Zhang, W. H. Liu, J. L. Yang, G. M. Zhou, Q. H. Yang and W. Lv, *ACS Nano*, 2023, **17**, 4453–4462.
35 Y. M. Y. Zhao, L. B. Li, H. Yang, S. B. Fan, S. Li and H. Tong, *Energy Storage Mater.*, 2024, **65**, 103126.
36 Z. G. Chen, W. M. Chen, H. X. Wang, C. Zhang, X. Q. Qi, L. Qie, F. S. Wu, L. Wang and F. Q. Yu, *Nano Energy*, 2022, **93**, 106836.
37 B. Jagger and M. Pasta, *Joule*, 2023, **7**, 2228–2244.
38 S. N. Zhang, Y. H. Li, L. J. Bannenberg, M. Liu, S. Ganapathy and M. Wagemaker, *Sci. Adv.*, 2024, **10**, eadj8889.
39 Z. J. Ju, C. B. Jin, X. H. Cai, O. W. Sheng, J. C. Wang, J. M. Luo, H. D. Yuan, G. X. Lu, X. Y. Tao and Z. Liang, *ACS Energy Lett.*, 2022, **8**, 486–493.
40 T. Duan, H. W. Cheng, Y. B. Liu, Q. C. Sun, W. Nie, X. G. Lu, P. P. Dong and M. K. Song, *Energy Storage Mater.*, 2024, **65**, 103091.
41 L. G. Yue, X. Y. Wang, L. Chen, D. J. Shen, Z. H. Shao, H. Wu, S. F. Xiao, W. Q. Liang, Y. J. Yu and Y. Y. Li, *Energy Environ. Sci.*, 2024, **17**, 1117–1131.
42 X. Z. Fan, J. H. Zhang, N. Yao, J. X. Chen, X. Chen and L. Kong, *Adv. Energy Mater.*, 2024, **14**, 2303336.
43 Z. H. Wu, C. Y. Wang, Z. Y. Hui, H. D. Liu, S. Wang, S. C. Yu, X. Xing, J. Holoubek, Q. S. Miao, H. L. Xin and P. Liu, *Nat. Energy*, 2023, **8**, 340–350.
44 G. X. Lu, Q. Q. Qiao, M. T. Zhang, J. S. Zhang, S. Li, C. B. Jin, H. D. Yuan, Z. J. Ju, R. Huang, Y. J. Liu, J. M. Luo, Y. Wang, G. M. Zhou, X. Y. Tao and J. Nai, *Sci. Adv.*, 2024, **10**, eado7348.
45 C. Y. Wang, C. P. Yang, Y. H. Du, Z. P. Guo and H. Ye, *Adv. Funct. Mater.*, 2023, **33**, 2303427.

46 X. R. Chen, Y. X. Yao, C. Yan, R. Zhang, X. B. Cheng and Q. Zhang, *Angew. Chem., Int. Ed.*, 2020, **59**, 7743–7747.
47 J. C. Guo, S. J. Tan, C. H. Zhang, W. P. Wang, Y. Zhao, F. Y. Wang, X. S. Zhang, R. Wen, Y. Zhang, M. Fan, S. Xin, J. Zhang and Y. G. Guo, *Adv. Mater.*, 2023, **35**, 2300350.
48 J. J. Pan, K. X. Shi, H. Wu, J. H. Li, R. Zhang, Q. B. Liu and Z. X. Liang, *Adv. Energy Mater.*, 2024, **14**, 2302862.
49 Z. Q. Shi, Y. M. Wang, X. Y. Yue, J. Zhao, M. M. Fang, J. J. Liu, Y. M. Chen, Y. T. Dong, X. Z. Yan and Z. Liang, *Adv. Mater.*, 2024, **36**, 2401711.
50 Y. Y. Zhang, Y. Guo, K. Yong, Q. Wang, M. Yao, Y. Zhang and H. Wu, *Energy Environ. Sci.*, 2024, **17**, 5819–5832.
51 H. Liu, F. X. Zhen, X. K. Yin, Y. B. Wu, K. L. Yu, X. P. Kong, S. J. Ding and W. Yu, *Angew. Chem., Int. Ed.*, 2025, **64**, e202414599.
52 J. Chen, X. T. Deng, X. Jia, Y. Gao, H. Chen, Z. Q. Lin and S. J. Ding, *J. Am. Chem. Soc.*, 2024, **146**, 30836–30847.
53 Z. H. Sun, Y. K. Wang, S. Y. Shen, X. Y. Li, X. F. Hu, M. Y. Hu, Y. Q. Su, S. J. Ding and C. H. Xiao, *Angew. Chem., Int. Ed.*, 2023, **62**, e202309622.
54 G. X. Lu, X. R. Wu, M. F. Huang, M. T. Zhang, Z. H. Piao, X. W. Zhong, C. Li, Y. Z. Song, C. S. Chang, K. Yu and G. M. Zhou, *Energy Environ. Sci.*, 2024, **17**, 9555–9565.
55 W. Wu, F. Niu, C. K. Sun, Q. R. Wang, M. Wang, J. Wang, Y. H. Deng, D. Ning, W. J. Li, J. Zhang, M. Chen, H. M. Cheng and C. L. Yang, *Adv. Mater.*, 2024, **36**, 2404630.
56 Y. P. Song, L. N. He, S. Zhang, X. Liu, K. Chen, Q. J. Jia, Z. H. Zhang and M. Du, *Food Chem.*, 2021, **351**, 129248.
57 J. P. Perdew, K. Burke and M. Ernzerhof, *Phys. Rev. Lett.*, 1996, **77**, 3865–3868.
58 G. Kresse and D. Joubert, *Phys. Rev. B: Condens. Matter Mater. Phys.*, 1999, **59**, 1758–1775.
59 S. Grimme, J. Antony, S. Ehrlich and H. Krieg, *J. Chem. Phys.*, 2010, **132**, 19.